

# Liquid–liquid phase transition in hydrogen by coupled electron–ion Monte Carlo simulations

Carlo Pierleoni<sup>a,1</sup>, Miguel A. Morales<sup>b</sup>, Giovanni Rillo<sup>c</sup>, Markus Holzmann<sup>d</sup>, and David M. Ceperley<sup>e,1</sup>

<sup>a</sup>Department of Physical and Chemical Sciences, University of L'Aquila, Via Vetoio 10, I-67010 L'Aquila, Italy; <sup>b</sup>Physics Division, Lawrence Livermore National Laboratory, Livermore, CA 94550; <sup>c</sup>Department of Physics, Sapienza University of Rome, 00185 Rome, Italy; <sup>d</sup>Laboratoire de Physique et Modélisation des Milieux Condensés, CNRS and Université Grenoble Alpes, F-38000 Grenoble, France; and <sup>e</sup>Department of Physics, University of Illinois at Urbana–Champaign, Champaign, IL 61801

Contributed by David M. Ceperley, March 15, 2016 (sent for review January 5, 2016; reviewed by Russell Hemley and Isaac F. Silvera)

**The phase diagram of high-pressure hydrogen is of great interest for fundamental research, planetary physics, and energy applications. A first-order phase transition in the fluid phase between a molecular insulating fluid and a monoatomic metallic fluid has been predicted. The existence and precise location of the transition line is relevant for planetary models. Recent experiments reported contrasting results about the location of the transition. Theoretical results based on density functional theory are also very scattered. We report highly accurate coupled electron–ion Monte Carlo calculations of this transition, finding results that lie between the two experimental predictions, close to that measured in diamond anvil cell experiments but at 25–30 GPa higher pressure. The transition along an isotherm is signaled by a discontinuity in the specific volume, a sudden dissociation of the molecules, a jump in electrical conductivity, and loss of electron localization.**

high pressure | phase transitions | quantum Monte Carlo | hydrogen metallization | molecular dissociation

Hydrogen is the simplest element of the periodic table and a paradigmatic element in developing general physical theories of condensed matter. Despite the simple electronic structure, its phase diagram is unexpectedly rich, ranging from the normal three-phase equilibria (solid–liquid–gas) of the low-pressure molecular system to the fully dissociated and ionized plasma states at extreme conditions of temperature and pressure. Accurate knowledge of its phase diagram is highly relevant as testified by the continuing intense research activity over the last half century (1–5). Its relevance in nature arises because it is the most abundant element in the universe and, together with the next simplest element helium, constitutes 70–90% of the atmosphere of the giant planets, Jupiter and Saturn, and of the many, recently discovered, exoplanets. Also, it is the putative element for nuclear fusion for energy applications.

The longest outstanding issue concerns the metal–insulator transition and its interplay with molecular dissociation. Molecular dissociation can occur either upon increasing temperature in the low-pressure fluid or upon increasing pressure in the low-temperature crystalline phase, or even as a combined action of temperature and pressure in the denser molecular fluid (5). The first prediction of metallization at zero temperature suggested that the molecular crystal would become atomic and transform to a simple metal above 25 GPa (1). Later experiments with higher pressures up to at least 360 GPa have found no convincing evidence of the metallic state at least below room temperature. However, they have revealed a rich phase diagram with a sequence of phase transformations in the molecular solid and the possibility of a semimetallic state (3, 6–13).

The metallic state has been unequivocally observed in the dense fluid in the range of 100–200 GPa and estimated temperatures of 2,000–3,000 K by dynamical compression experiments (5, 14–16). Using the reverberating shock wave method, Weir et al. (15) and Nellis (14) measured a drop of resistivity with pressure down to  $\sim 500$  ( $\mu\Omega$  cm) at 140 GPa for hydrogen. At higher pressures the resistivity was roughly constant, signaling

the metallic state. A transition temperature of  $\sim 2,600$  K was estimated using a model equation of state (EOS). Measuring the compressibility of reverberating shocked deuterium, Fortov et al. (16) measured a 20% increase of the density of the liquid in the regime where previous experiments on hydrogen (15, 17–19) have detected a sharp increase of conductivity of roughly 5 orders of magnitude, supporting the idea that dissociation and metallization occur simultaneously. However, the data were too sparse to establish the presence of a phase transition. Again, temperature estimated by models located the experimental points between 2,500 and 4,000 K, whereas using the EOS from ab initio calculations provides a temperature between 1,500 and 2,000 K (5).

A liquid–liquid phase transition (LLPT) has been predicted by theory to occur below a critical temperature of  $\sim 2,000$  K (20). In the last year important and contrasting experimental and theoretical contributions have appeared concerning the LLPT.

On the experimental side new experiments have been performed, both by static compression methods within a diamond anvil cell (DAC) and laser pulses to heat the sample and reach the liquid state (21–23), and by dynamical compression methods with suitably shaped laser ramps to generate the shock wave suitable to follow the transition line (24). The two sets of experiments reached quite different conclusions. The static experiments using hydrogen detected a signature of a first-order transition and metallization at moderately low pressure ( $\sim 150$  GPa) by detecting a plateau in the temperature–laser power curve and a change in reflectivity from that characteristic of an insulator to that characteristic of a conductor. The dynamical experiment using deuterium also detected the signature of metallization by observing a sudden increase in

## Significance

**Understanding hydrogen metallization under pressure and its interplay with molecular dissociation is still a major challenge in high-pressure and fundamental physics. We report results of quantum Monte Carlo simulations that indicate that the two phenomena occur simultaneously through a first-order phase transition in fluid hydrogen at megabar pressures and temperatures of 1,000 K. The predicted pressures are close to claims of metallization based on static compression experiments but are lower than that of recent dynamic compression measurements. The simulation results represent the most reliable theoretical prediction yet of the liquid–liquid transition in hydrogen and provide constraints for future experiments.**

Author contributions: C.P., M.A.M., M.H., and D.M.C. designed research; C.P. and G.R. performed research; C.P., M.A.M., G.R., M.H., and D.M.C. analyzed data; C.P., M.A.M., G.R., M.H., and D.M.C. developed the code; and C.P., M.H., and D.M.C. wrote the paper.

Reviewers: R.H., Carnegie Institution of Washington; and I.F.S., Harvard University.

The authors declare no conflict of interest.

Freely available online through the PNAS open access option.

<sup>1</sup>To whom correspondence may be addressed. Email: carlo.pierleoni@aquila.infn.it or ceperley@uiuc.edu.

This article contains supporting information online at [www.pnas.org/lookup/suppl/doi:10.1073/pnas.1603853113/-DCSupplemental](http://www.pnas.org/lookup/suppl/doi:10.1073/pnas.1603853113/-DCSupplemental).

reflectivity but at much higher pressure ( $\sim 300$  GPa) along an almost temperature-independent line. The dissociated character of the fluid was inferred by using ab initio theory.

On the theoretical side, the occurrence of a first-order transition between two liquids of different character was conjectured a long time ago based on various methods (25–27), by ab initio simulations (28, 29) and more recently firmly established within the first-principles molecular dynamics (FPMD) with density functional theory (DFT) (20, 24, 30–32). Within this theory the exact location of the transition line depends on the specific approximation adopted for the exchange–correlation (X-C) functional: semilocal functionals like Perdew–Burke–Ernzerhof (PBE) predicting lower transition pressures than the van-der-Waals–corrected functionals (vdW-DF and vdW-DF2), with the prediction of the nonlocal hybrid Heyd–Scuseria–Ernzerhof (HSE) functional lying somewhat between the two sets. The location of the transition line ranges from 100 to 400 GPa. Nuclear quantum effects, considered both explicitly by path integral methods (30) and by approximate theories (24), reduce the transition pressure by  $\sim 10$ –20% (depending on the temperature) with respect to calculations for classical protons. Results obtained using the coupled electron–ion Monte Carlo (CEIMC) method (20, 33) also supported the existence of a first-order phase transition in agreement with FPMD, although the location of the transition line was different. In CEIMC the electronic problem is solved by quantum Monte Carlo (QMC), which is formulated directly in terms of electrons and protons, and thus a more fundamental description of correlation (5, 34). QMC is more accurate than DFT and because of its variational character the relative accuracy of various approximations can be established. In contrast, establishing the relative accuracy of various approximations within DFT requires predictions from a more fundamental theory or from experiments. Recently, a different QMC-based method (MD-QMC) has been exploited to investigate high-pressure liquid hydrogen (35, 36). This new method predicted the occurrence of two distinct phase transitions, a nonmetal to metal transition at lower pressure (from 150 to 450 GPa depending on temperature) between a purely molecular-insulating phase and a mixed molecular-atomic and metallic phase of liquid hydrogen, and a second dissociation transition at higher pressure (from 400 to 600 GPa depending on temperature). This disagrees both with experiments and previous theories and is not confirmed by our calculations based on more accurate treatment of finite-size effects and better trial wave functions as discussed below.

Here we report results of an extensive study of the LLPT and the properties of the liquid in the transition region by CEIMC. With respect to our previous studies, we have an improved trial wave function using several types of orbitals, a much more extensive set of data (more isotherms and a wider range of densities), and we consider both classical and quantum protons. We carefully investigate and correct for all main sources of bias affecting the results. Our present results, summarized and compared with the recent experiments in Fig. 1, confirm the picture of a unique LLPT where molecular dissociation and metallization occur simultaneously. The location of the transition line lies between the two experimental results, at only 25–30 GPa higher pressure than the DAC experimental data. Also, the shapes of DAC-derived and CEIMC-predicted lines are similar: they both exhibit a change of curvature for increasing pressure, clearly detectable despite the sparse grid of temperatures investigated. The origin of such change of behavior is unclear at present. The transition measured in the dynamical experiments instead is located at higher pressure and it is almost temperature independent. (Note that the DAC experiment used hydrogen and should be compared with our line at lower pressure whereas the dynamical compression experiment used deuterium and should be compared with our line at higher pressure.) At present the origin of the disagreement

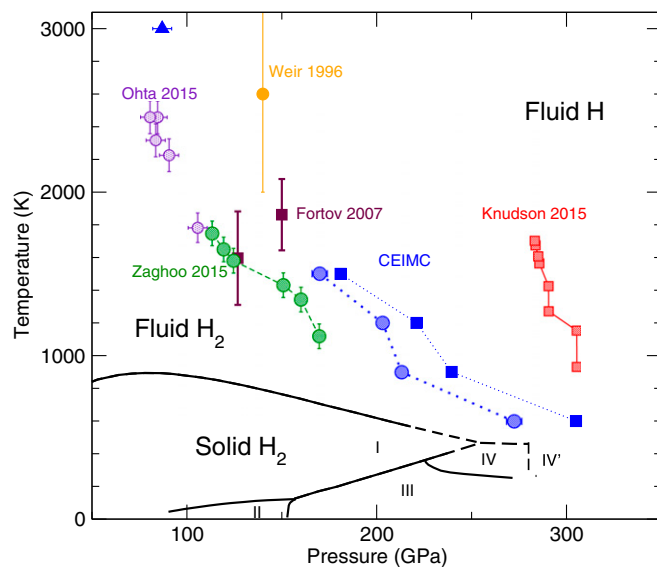


**Fig. 1.** Hydrogen phase diagram with experimental liquid–liquid transition lines and CEIMC predictions. Black continuous lines indicate the melting line as well as the transition lines between different experimentally detected (3, 13) crystalline phases: I–IV. Melting line of phase IV and the new phase IV', indicated by dashed black lines, are still speculative (13). Blue circles and squares are CEIMC predictions for the liquid–liquid transition line in hydrogen and in deuterium, respectively. DAC experimental results for hydrogen are indicated by green circles (22) and purple circles (23), whereas red squares indicate shock wave experimental data for deuterium (24). We also report an earlier experimental point for the conductivity onset in liquid hydrogen (yellow circle) (15) and two points for deuterium dissociation and metallization (maroon squares) (16). The error bars on the temperature for the latter two sets of data reported here were inferred from theories (5). In fact, all dynamical experiments (15, 16, 24) used models to determine  $T$ . The blue triangle at 3,000 K indicates the CEIMC prediction for a metallization cross-over above the critical point where the conductivity is  $2 - 4 \times 10^3 (\Omega \text{ cm})^{-1}$ .

between the two experiments is unclear, as well as the origin of the shift between our predictions and the experimental lines.

We have studied the systems of both classical and quantum protons along five isotherms:  $T = 600, 900, 1,200, 1,500,$  and  $3,000$  K. We explicitly avoid isotherms close to the predicted critical point (2,000 K) because we expect critical fluctuations and size effects to hamper an accurate location of the transition. Fig. 2 illustrates the results along the  $T = 600$  K isotherm for classical protons. It is illustrative of the results for all isotherms except  $T = 3,000$  K where no transition is observed. In Fig. 2A we report the EOS in terms of  $r_s$  vs. pressure. The occurrence of a discontinuity with two distinct branches, and two coexisting densities at the transition is evident. We report both the raw data (black diamonds) and the size-corrected data (red circles) and show that size effects, although not negligible, are very limited and push the transition pressure to  $\sim 5\%$  higher values (see the *SI Appendix* for a more extensive discussion). The observed discontinuity is a clear signature of a first-order phase transition with an associated latent heat. In all cases, and in agreement with previous work (20), we observe a small specific volume jump at the transition and the absence of detectable metastable states along the two branches of the EOS. These features of a weakly first-order transition allow us to accurately locate the transition pressure without the need to compare free energies of the coexisting phases.

The values of the transition pressure along the various isotherms obtained with this method are reported in Fig. 1 for hydrogen treated quantum mechanically; the data for deuterium are obtained by interpolating results from classical and quantum

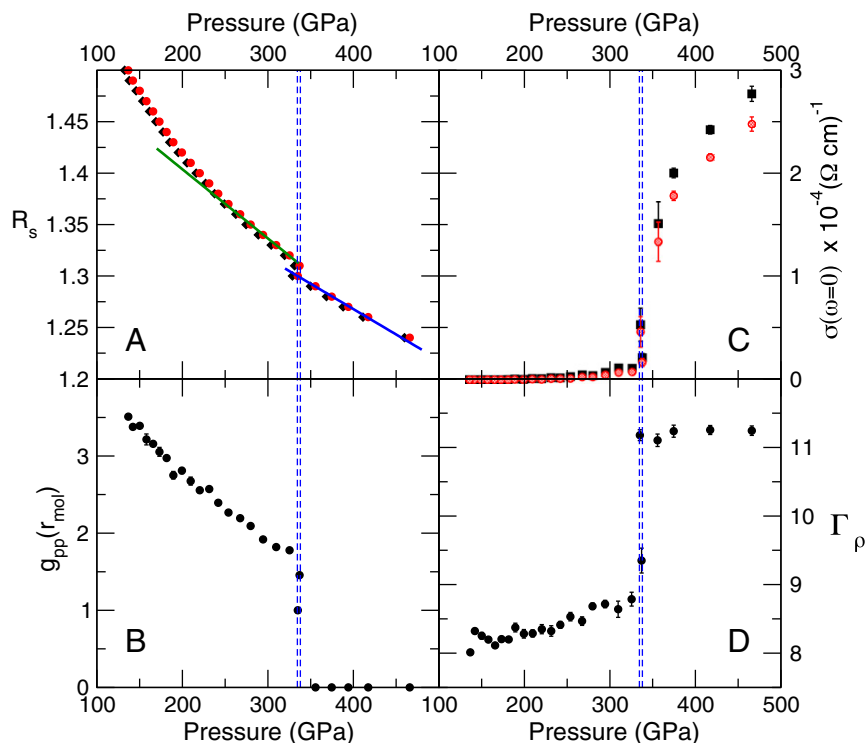


**Fig. 2.** Results for the system with classical protons along the  $T = 600$  K isotherm. (A, Upper Left) EOS expressed by the coupling parameter  $r_s$  versus the pressure. Raw data (black diamonds) and size-corrected results (red circles) are reported, together with linear fits for the two branches near the discontinuity. Note that below  $\sim 200$  GPa our EOS is for the metastable fluid because the thermodynamically stable state should be the phase I crystal. (B, Lower Left) Amplitude of the molecular peak observed in the proton–proton radial distribution functions  $g_{pp}(r_{mol})$ , where  $r_{mol} \simeq 1.4a_0$ . Beyond the vertical blue lines,  $g_{pp}(r)$  do not exhibit a maximum but only a shoulder at the molecular distance. (C, Upper Right) dc electrical conductivity as obtained by optical calculation within DFT with two X-C approximations (black squares, PBE; red circles, vdW-DF). The points are averages over 10 statistically independent nuclear configurations sampled during the CEIMC run at each density. (D, Lower Right) Integral of the absolute value of the single-electron off-diagonal density matrix from variational Monte Carlo, as a measure of the electron localization, obtained by averaging over 10 independent nuclear configurations. In all panels the blue vertical dashed lines represent the transition pressure with its uncertainty.

protons. From the slope of the two branches of the EOS at the transition (indicated by linear segments in Fig. 2A) we extracted the isothermal compressibility of the coexisting phases. We find that the lower pressure phase is  $\sim 15$ – $30\%$  more compressible than the higher pressure phase, the effect being slightly larger for classical nuclei than for quantum protons. Moreover, the critical compressibility is found to increase roughly linearly with temperature along the transition line from  $\sim 1.5 \times 10^{-3}$  to  $\sim 3.0 \times 10^{-3}$  a.u. in the range  $T = 600$ – $1,500$  K. Finally, the critical compressibility of quantum hydrogen is  $\sim 20\%$  larger than for classical nuclei because of the lower transition pressure of quantum hydrogen. The direct observation of the transition pressure allows us to extract the latent heat of the transition as the difference of the enthalpy per atom between the coexisting phases at the transition pressure. The estimated latent heat,  $630(150)$  K, is in agreement with previous estimate (20) and is roughly constant in the range  $600$ – $1,500$  K. See the *SI Appendix* for more details.

Concerning structural properties, we observe a mostly molecular phase (lower density) in coexistence with a mostly atomic phase (higher density) at the transition pressure. This is signaled by the amplitude of the molecular peak in the proton–proton pair-correlation functions  $g_{pp}(r_{mol})$ , where  $r_{mol} \simeq 1.4a_0$  as illustrated in Fig. 2B. Note that the two coexisting points have a mixed character but the adjacent pressures are fully characterized as molecular (lower density) and atomic (higher density). This is at variance with recent results from FPMD using vdW-DF2 approximation, where the molecular character persists in the high-pressure phase well beyond the transition pressure (see the supporting information of ref. 24). The structure of the high-

pressure phase is peculiar because protons can still be found at distance of the molecular bond ( $\sim 1.4a_0$ ), although with a reduced probability with respect to the low-pressure phase. However, analysis of the dynamics reveals that the protons change partners easily, a clear indication that a molecular description is not appropriate for these thermodynamic states.

The electronic properties of the coexisting phases can be characterized in several ways. Here we report the calculation of the electrical conductivity as obtained using the Kubo–Greenwood formula with well-converged DFT orbitals and nuclear configurations sampled during the CEIMC runs. The results for the dc conductivity, obtained by averaging over 10 statistically independent nuclear configurations, and obtained by Kohn–Sham orbitals from PBE and vdW-DF1 X-C approximations, are reported in Fig. 2C. The quantitative value of the conductivity depends on the DFT approximation but the sudden appearance of the metallic character at the transition pressure is clear: The two coexisting points both show a nonvanishing signal supporting our observation of a mixed character, but the adjacent densities are insulating at lower pressure or metallic at higher pressure.

An alternative way to characterize the electronic state is through the reduced single-electron density matrix  $\rho^{(1)}(\mathbf{r}, \mathbf{r}') = \langle \psi^\dagger(\mathbf{r})\psi(\mathbf{r}') \rangle$ , where  $\psi^\dagger(\mathbf{r})$  and  $\psi(\mathbf{r}')$  are, respectively, creation and annihilation operators and  $\langle \dots \rangle$  denotes the integral over the electronic wave function and over nuclear configurations. At the insulator-to-metal transition the envelope of the curve, a measure of the electron localization in real space, should change from an exponential to an

algebraic decay. Following ref. 36, we compute the following integral over the simulation cell:

$$\Gamma_\rho = \frac{1}{N} \int_V \frac{d\mathbf{r}d\mathbf{r}'}{V} \left| \rho^{(1)}(\mathbf{r}, \mathbf{r}') \right|, \quad [1]$$

as shown in Fig. 2D. Whereas in the insulating phase  $\Gamma_\rho$  weakly increases with pressure, it is constant in the metallic phase, and a clear jump is observed at the transition. This discontinuity reflects a clear change of behavior in the integrand at the transition. Although an  $8 \times 8 \times 8$  grid of twist angles is used for these calculations, the size of our systems is too small to saturate the integral even in the insulating phase. This reflects the residual itinerant character of the electrons in the molecular liquid near metallization.

In Fig. 3 we report our data for the transition lines together with predictions from FPMD simulations with different DFT approximations (24) and previous QMC-based results (20, 33, 35, 36). We report transition lines from four different X-C approximations, namely PBE, HSE, vdW-DF, and vdW-DF2, and for both classical and quantum protons. For each functional (except for HSE), the line at higher pressure corresponds to classical nuclei, whereas the line at lower pressure corresponds to quantum protons. The general trend of the DFT approximations is quite clear. GGA-PBE favors the dissociated-metallic phase followed by HSE, then by vdW-DF, and finally by vdW-DF2. The difference in pressure between GGA-PBE and vdW-DF2 is as much as 250 GPa. The CEIMC data lie between the two extremes and in rough agreement with the vdW-DF and HSE approximations. This was expected on the basis of a detailed analysis of functional performance (37). However, even in

these cases the agreement is only qualitative; e.g., the HSE line for classical nuclei describes well the classical CEIMC data at lower temperature but is too low in pressure at higher temperature. On the other hand, vdW-DF for quantum hydrogen agrees with CEIMC at high temperature but overestimates the transition pressure at lower temperature. In general, none of the DFT curves exhibits the change of curvature of the transition line observed for CEIMC and for the static compression data. Fig. 3 also shows CEIMC results of a previous investigation (20, 33), which however have been found to be biased by nonconverged orbitals (38).

Finally, in Fig. 3 we report recent results from MD-QMC which, as mentioned above, have predicted two different transitions, the first one ascribed to the insulator–metal transition (IMT in the figure) (36), the second one, at higher pressure, associated with the molecular dissociation transition (35). It is important to discuss the reason for such large disagreement because both our present work and the above-mentioned work are based on QMC methods. In the supporting information of ref. 36, a quantitative comparison between the trial wave functions for selected configurations was reported. The present trial wave function (DFT orbitals + two-body and three-body Jastrow + backflow) is shown to have a lower energy with respect to the trial function used in refs. 35, 36. However, we believe that the largest contribution to the disagreement arises from the different treatment of size effects in the two studies. Here we used small systems (54 and 128 protons) with twist-averaged boundary conditions (TABC), while in refs. 35 and 36 larger systems (up to 256 protons) at the  $\Gamma$ -point were considered. As discussed in ref. 20, size effects in hydrogen, in particular near metallization, are quite large and required systems of 432 atoms or larger at the  $\Gamma$ -point for an accurate location of the transition. Conversely, smaller systems require  $k$ -point sampling to exhibit the transition. This picture, seen in both DFT and QMC simulations, is the largest contribution to the finite-size corrections (39) (*SI Appendix*). The purely electronic origin of the leading finite-size effects is consistent with the residual itinerant character of the electrons found in both phases and reveals a slow decay of the single-electron density matrix with distance. Another source of bias is the use of localized orbitals in refs. 35, 36 which favor the molecular-insulating phase over the atomic-metallic phase, hence separating the two phenomena (metallization and dissociation) and pushing the transition lines to higher pressures.

In conclusion, we have reported what we believe are the most accurate predictions for the location of the liquid–liquid transition line in high-pressure hydrogen. We confirm the existence of a single transition at which metallization and molecular dissociation simultaneously occur. Our prediction is 25–30 GPa higher in pressure than recent experimental results from static compression techniques (22). Note that in those experiments the pressure is measured at ambient temperature only, i.e., in the crystal phase I, and used at higher pressure in the liquid phase. This might be a possible origin of the disagreement with our predictions. On the other hand, recent shock wave experiments located the transition line at a higher pressure and almost independent of temperature (24), in striking disagreement with DAC experiments and with our predictions. The origin of this disagreement remains unclear. Our predictions are far more reliable than DFT-based predictions of the transition line and should be considered a better theoretical reference.

## Materials and Methods

Using constant volume simulations we have studied dense hydrogen along five isotherms at 3,000, 1,500, 1,200, 900, and 600 K for a range of densities around the transition. We used the CEIMC method, an ab initio method in which the nuclear configuration space is explored by Metropolis Monte Carlo, and the Born–Oppenheimer potential energy surface is provided by

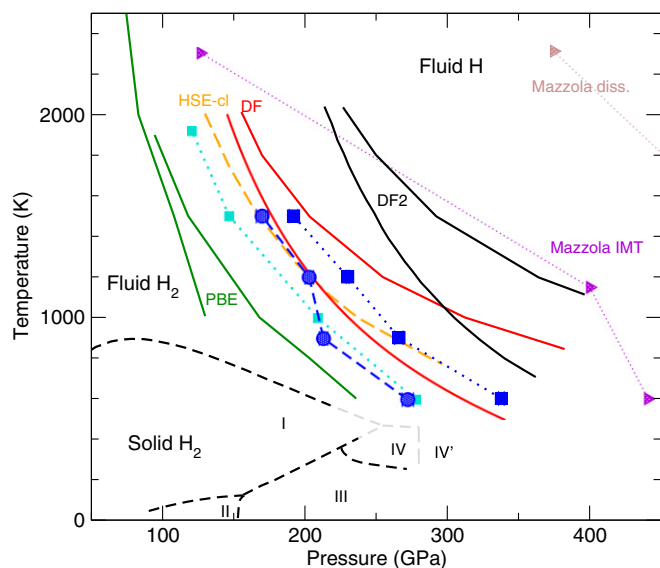


**Fig. 3.** Comparison of CEIMC results for the transition line with previous theoretical predictions. Blue circles and squares are CEIMC transition pressures for hydrogen and systems with classical protons, respectively. Continuous lines are predictions from FPMD with different X-C approximations: vdW-DF2 (black lines), vdW-DF (red lines), GGA-PBE (green lines), HSE (orange dashed line). For each approximation, except HSE, the line at lower pressure corresponds to quantum protons whereas the line at higher pressure corresponds to classical protons. For HSE only the classical protons line (from ref. 24) is shown. Triangles are predictions for metallization (violet) and molecular dissociation (brown) from MD-QMC (35, 36). Earlier (unconverged) CEIMC data for classical protons are also reported as cyan squares (20, 33). Transition lines for the crystalline phases are shown by dashed lines (see Fig. 1 legend).

ground-state QMC for the electronic degrees of freedom. We mostly used systems of 54 nuclei and 54 electrons. The use of twist-averaged boundary conditions (TABC) during the nuclear sampling eliminates the dominating size effects stemming from the (almost) itinerant character of the electrons. Subleading size effects after TABC do not strongly affect nuclear sampling, allowing a post-processing of the data to extrapolate to the thermodynamic limit (39). As an independent check for possible finite-size bias, we have investigated systems of 128 protons and electrons at selected points (*SI Appendix*).

Calculations of optical properties were performed for CEIMC-generated nuclear configurations within DFT, using a plane-wave energy cutoff of 1360 eV, an  $8 \times 8 \times 8$  Monkhorst–Pack grid of  $k$  points, a smearing of 0.086 in the self-consistent cycle, and a smearing of 0.3 eV to regularize the frequency-dependent conductivity. The dc conductivity has been estimated by fitting a Drude curve to the DFT data when appropriate. The number of bands was set to 64 and 120 for systems of 54 and 128 electrons, respectively.

- Wigner E, Huntington HB (1935) On the possibility of a metallic modification of hydrogen. *J Chem Phys* 3:764–770.
- Silvera IF (1980) The solid molecular hydrogens in the condensed phase: Fundamentals and static properties. *Rev Mod Phys* 62(2):393–452.
- Mao HK, Hemley RJ (1994) Ultrahigh-pressure transitions in solid hydrogen. *Rev Mod Phys* 66(2):671–692.
- Maksimov EG, Shilov YI (1999) Hydrogen at high pressure. *Phys Uspekhi* 42(11):1121–1138.
- McMahon JM, Morales MA, Pierleoni C, Ceperley DM (2012) The properties of hydrogen and helium under extreme conditions. *Rev Mod Phys* 84(4):1607–1653.
- Loubeyre P, Occelli F, LeToullec R (2002) Optical studies of solid hydrogen to 320 GPa and evidence for black hydrogen. *Nature* 416(6881):613–617.
- Howie RT, Guillaume CL, Scheler T, Goncharov AF, Gregoryanz E (2012) Mixed molecular and atomic phase of dense hydrogen. *Phys Rev Lett* 108(12):125501.
- Eremets MI, Troyan IA (2011) Conductive dense hydrogen. *Nat Mater* 10(12):927–931.
- Zha CS, Liu Z, Hemley RJ (2012) Synchrotron infrared measurements of dense hydrogen to 360 GPa. *Phys Rev Lett* 108(14):146402.
- Zha CS, Liu Z, Ahart M, Boehler R, Hemley RJ (2013) High-pressure measurements of hydrogen phase IV using synchrotron infrared spectroscopy. *Phys Rev Lett* 110(21):217402.
- Cohen RE, Naumov II, Hemley RJ (2013) Electronic excitations and metallization of dense solid hydrogen. *Proc Natl Acad Sci USA* 110(34):13757–13762.
- Zha CS, Cohen RE, Mao HK, Hemley RJ (2014) Raman measurements of phase transitions in dense solid hydrogen and deuterium to 325 GPa. *Proc Natl Acad Sci USA* 111(13):4792–4797.
- Howie RT, Dalladay-Simpson P, Gregoryanz E (2015) Raman spectroscopy of hot hydrogen above 200 GPa. *Nat Mater* 14(5):495–499.
- Nellis WJ (2006) Dynamic compression of materials: Metallization of fluid hydrogen at high pressures. *Rep Prog Phys* 69:1479–1580.
- Weir ST, Mitchell AC, Nellis WJ (1996) Metallization of fluid molecular hydrogen at 140 GPa (1.4 Mbar). *Phys Rev Lett* 76(11):1860–1863.
- Fortov VE, et al. (2007) Phase transition in a strongly nonideal deuterium plasma generated by quasi-isentropic compression at megabar pressures. *Phys Rev Lett* 99(18):185001.
- Ternovoi VY, et al. (1999) Thermodynamic properties and electrical conductivity of hydrogen under multiple shock compression to 150 GPa. *Physica B* 265(1–4):6–11.
- Fortov VE, et al. (2003) Pressure-produced ionization of nonideal plasma in a megabar range of dynamic pressures. *Sov Phys JETP* 97(2):259–278.
- Nellis WJ, Weir ST, Mitchell AC (1999) Minimum metallic conductivity of fluid hydrogen at 140 GPa (1.4 Mbar). *Phys Rev B* 59(5):3434–3449.
- Morales MA, Pierleoni C, Schwegler E, Ceperley DM (2010) Evidence for a first-order liquid-liquid transition in high-pressure hydrogen from ab initio simulations. *Proc Natl Acad Sci USA* 107(29):12799–12803.
- Dzyabura V, Zaghou M, Silvera IF (2013) Evidence of a liquid-liquid phase transition in hot dense hydrogen. *Proc Natl Acad Sci USA* 110(20):8040–8044.
- Zaghou M, Salamat A, Silvera IF (2015) A first-order phase transition to metallic hydrogen. arXiv:1504.00259.
- Ohta K, et al. (2015) Phase boundary of hot dense fluid hydrogen. *Sci Rep* 5:16560.
- Knudson MD, et al. (2015) High-pressure physics. Direct observation of an abrupt insulator-to-metal transition in dense liquid deuterium. *Science* 348(6242):1455–1460.
- Norman G, Starostin A (1968) Insufficiency of classical description of a nondegenerate dense plasma. *High Temp* 6:394–399.
- Ebeling W, Richter W (1985) Plasma phase-transition in hydrogen. *Phys Lett A* 108(2):80–82.
- Saumon D, Chabrier G (1989) Fluid hydrogen at high density: The plasma phase transition. *Phys Rev Lett* 62(20):2397–2400.
- Magro WR, Ceperley DM, Pierleoni C, Bernu B (1996) Molecular dissociation in hot, dense hydrogen. *Phys Rev Lett* 76(8):1240–1243.
- Scandolo S (2003) Liquid-liquid phase transition in compressed hydrogen from first-principles simulations. *Proc Natl Acad Sci USA* 100(6):3051–3053.
- Morales MA, McMahon JM, Pierleoni C, Ceperley DM (2013) Nuclear quantum effects and nonlocal exchange-correlation functionals applied to liquid hydrogen at high pressure. *Phys Rev Lett* 110(6):065702.
- Lorenzen W, Holst B, Redmer R (2010) First-order liquid-liquid phase transition in dense hydrogen. *Phys Rev B* 82(19):195107.
- Lorenzen W, Becker A, Redmer R (2014) Progress in warm dense matter and planetary physics *Frontiers and Challenges in Warm Dense Matter*, Lecture Notes in Computational Science and Engineering, eds Graziani F, Desjarlais MP, Redmer R, Trickey SB (Springer, Switzerland), Vol 96, pp 203–234.
- Liberatore E, Morales MA, Ceperley DM, Pierleoni C (2011) Free energy methods in coupled electron ion Monte Carlo. *Mol Phys* 109(23–24):3029–3036.
- Foulkes WMC, Mitas L, Needs RJ, Rajagopal G (2001) Quantum Monte Carlo simulation of solids. *Rev Mod Phys* 73(1):33–83.
- Mazzola G, Yunoki S, Sorella S (2014) Unexpectedly high pressure for molecular dissociation in liquid hydrogen by electronic simulation. *Nat Commun* 5:3487.
- Mazzola G, Sorella S (2015) Distinct metallization and atomization transitions in dense liquid hydrogen. *Phys Rev Lett* 114(10):105701.
- Clay RCI, et al. (2014) Benchmarking exchange-correlation functionals for hydrogen at high pressures using quantum Monte Carlo. *Phys Rev B* 89(18):184106.
- Morales MA, Clay RCI, Pierleoni C, Ceperley DM (2013) First principles methods: A perspective from quantum Monte Carlo. *Entropy (Basel)* 16(1):287–321.
- Holzmann M, et al. (2016) Theory of finite size effects for electronic quantum Monte Carlo calculations of liquids and solids. arXiv:1603.03957.

A complete report of technical details of our calculations and a detailed analysis of all biasing effects and corrections is provided in the *SI Appendix*.

**ACKNOWLEDGMENTS.** We would like to dedicate this work to Peri who has been so important for this collaboration. She will always remain in our hearts. M.H. and C.P. thank the Theory Group at ILL Grenoble for hospitality. C.P. was partially supported by the Italian Institute of Technology under the SEED project 259 SIMBEDD. M.A.M. was supported through the Predictive Theory and Modeling for Materials and Chemical Science program by the US Department of Energy (DOE) Office of Science, Basic Energy Sciences. This work was performed in part under the auspices of the US DOE by Lawrence Livermore National Laboratory under Contract DE-AC52-07NA27344. D.M.C. was supported by DOE Grant NA DE-NA0001789 and by the Fondation NanoSciences (Grenoble). Computer time was provided by PRACE Projects 2011050781 and 2013091918 and by an allocation of the Blue Waters sustained-petascale computing project, supported by the National Science Foundation (Award OCI 07-25070) and the State of Illinois.

**Supporting Information for:  
Liquid-liquid phase transition in hydrogen by Coupled Electron-Ion Monte  
Carlo Simulations**

Carlo Pierleoni<sup>1,\*</sup>, Miguel A. Morales<sup>2</sup>, Giovanni Rillo<sup>3</sup>, Markus Holzmann<sup>4</sup>, David M. Ceperley<sup>5</sup>

<sup>1</sup> *Department of Physical and Chemical Sciences,*

*University of L'Aquila, Via Vetoio 10, I-67010 L'Aquila, Italy*

<sup>2</sup> *Physics Division, Lawrence Livermore National Laboratory, California USA*

<sup>3</sup> *Department of Physics, Sapienza University of Rome, Italy*

<sup>4</sup> *LPMMC, CNRS and Université Grenoble Alpes, F-38000 Grenoble, France*

<sup>5</sup> *Department of Physics, University of Illinois Urbana-Champaign, USA*

(Dated: Friday 8<sup>th</sup> April, 2016)

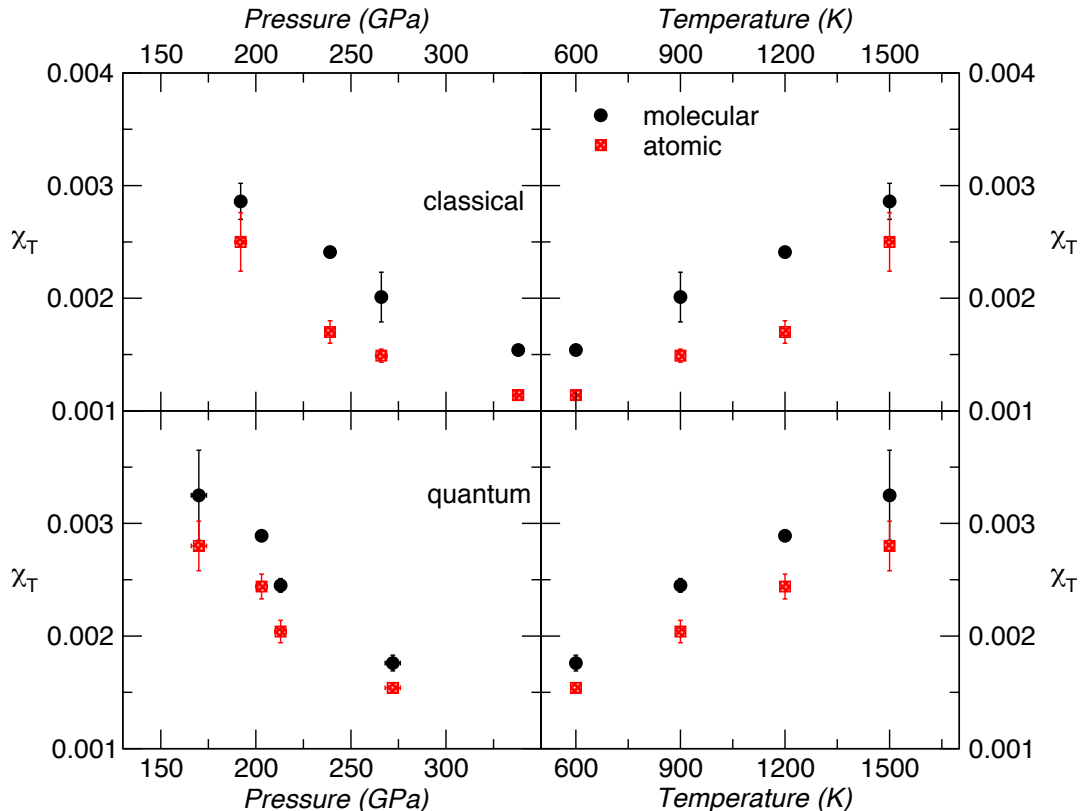


FIG. 1. (color online) Isothermal compressibility  $\chi_T(a.u.)$  of the coexisting phases for the system with classical protons (upper panels) and the system with quantum protons (lower panels), as function of pressure (left panels) and temperature (right panels). In each panel the mostly molecular phase (black circles) is compared to the mostly atomic phase (red squares).

## THERMODYNAMIC PROPERTIES

### Isothermal compressibility at the transition

Here we report results for the isothermal compressibility, defined as

$$\chi_T = -\frac{1}{v} \left( \frac{\partial v}{\partial p} \right)_{T,N} = -\frac{3}{r_s} \left( \frac{\partial r_s}{\partial p} \right)_{T,N} \quad (1)$$

of the two co-existing phases along the various isotherms. As mentioned in the main text, the compressibility of each phase is obtained by the slope of the corresponding branch of the EOS at the transition point. In Figure 1 we report the compressibility at the transition for the system with classical protons (upper panels) and the system with quantum protons (lower panels). In each panel we compare results for the mainly molecular (black circles) and mainly atomic (red squares) phases. We note that for both classical and quantum systems, the molecular phase is slightly more compressible than the coexisting monoatomic phase, and the compressibility increases roughly linearly with temperature and decreases roughly linearly with pressure, in the ranges investigated. Note how error bars are larger at largest temperature since fluctuations increase when approaching the critical point.

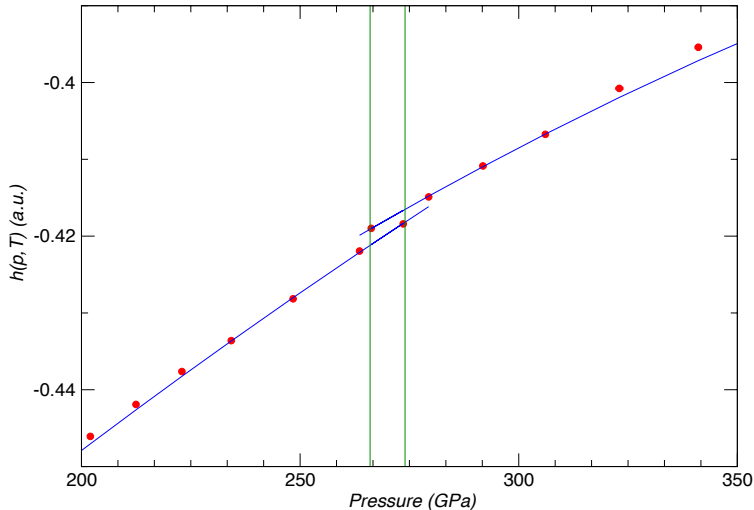


FIG. 2. (color online) T=600K quantum protons. Specific enthalpy versus pressure. Red circles are simulation data. The blue straight lines are linear fits in the two phases of the system near the transition point (we consider 4 points in each phase). The two vertical green lines indicate the range of pressure where the transition is observed.

### Latent heat

Since we have a direct determination of the transition pressure (see Figure 2 of the main text), we can estimate the difference of specific enthalpy  $h$  at coexistence, hence the latent heat of the transition  $\lambda_T$ . From thermodynamics  $g = h - Ts = e + pv - Ts$ , where  $g$  is the specific Gibbs free energy,  $s$  the specific entropy and  $e$  the specific internal energy. At the coexistence between phases I and II,  $\Delta g = g^I - g^{II} = 0$  so that  $\lambda_T = T\Delta s = T(s^I - s^{II}) = \Delta h = (h^I - h^{II})$ . Figure 2 illustrates the procedure for the system with quantum protons along the T=600K isotherm. Figure 3 reports the extracted values of the latent heat for both classical and quantum protons. Assigning a statistical uncertainty to those data is rather difficult since they come from subtracting fits for the two branches of the EOS. Using the standard rule of error propagation provides much too large error bars (200%) which clearly overestimate the uncertainty. Improving the accuracy of this determination requires a more accurate determination of the transition pressure through a finer density grid. Therefore in the main text we quote the observed data dispersion as an estimate of the error bar which implies that the latent heat is almost temperature independent and also does not depend, within our accuracy, on the quantum character of the protons.

### SIMULATION PROTOCOL

In CEIMC, the equilibrium Boltzmann distribution of nuclei, either represented as classical point particles or as quantum path integrals [1], is sampled by a Metropolis Monte Carlo procedure in which the Born-Oppenheimer energy is obtained by a separate Quantum Monte Carlo calculation for the ground state electrons at fixed nuclear positions. The method has been extensively reviewed in ref. [2] where the various ingredients have been discussed in details. Here we describe the protocol employed in the present work which is similar to the one adopted in a recent study of the deuterium Hugoniot [3]. The nuclear sampling is performed using variational Quantum Monte Carlo electronic energies. This allows an efficient exploration of the nuclear configuration space. Over the past few years we have developed an accurate Slater-Jastrow trial wave function [4-6]. The Jastrow term is the sum of one-body (electron-proton), two-body (electron-electron) and three-body correlation terms. We employ the analytical expressions from RPA [4] with additional empirical

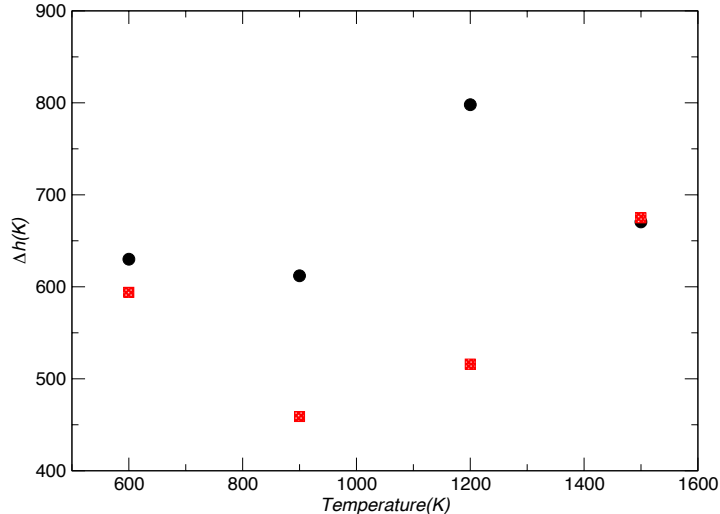


FIG. 3. (color online) Latent heat  $\lambda_T(K)$  versus temperature for classical protons (black dots) and quantum protons (red squares).

functions that preserve the short and long-range limits but introduce a few more variational parameters. The Slater determinant uses Kohn-Sham (KS) orbitals from DFT. We employ the PW solver from QuantumEspresso suite[7] using several different exchange-correlation (XC) approximations. Most of our calculations are performed with orbitals from the GGA-PBE approximation, however we have investigated the effect of changing the XC approximation as reported later in this Supplemental Material. We always use an energy cut-off of 40Ry within the DFT calculation but we correct the orbitals by using the exact electron-proton cusp as explained in ref. [5].

A backflow transformation is applied to the electron coordinates in the orbitals of the Slater determinants. The backflow transformation has both short and long range contributions; the analytic expression is complemented by an *ad hoc* short range function with optimized variational parameters [5, 8]. Adding an extra such term for both the Jastrow and the backflow functions decreases the energy by  $\sim 1mH/atom$  and the variance per electron by  $\sim 40\%$  (see below) without impacting the computer time.

In principle, the variational parameters should be optimized for each nuclear configuration but this will cause a large increase in computational time. Instead, at each fixed density, fixed number of particles and given type of KS orbitals, we select a number of statistically independent nuclear configurations (typically 32), generated with an unoptimized trial function. We then optimize the variational parameters for each configuration independently using a correlated sampling procedure. Then we determine the average for each parameter with respect to the nuclear configurations. This procedure takes into account the variation of the parameters with density and number of particles but they are not tailored for the specific configuration. We have checked that using average values of the variational parameters provides a difference of  $\sim 0.02mH/atom$  in the internal energy and of  $\sim 0.03GPa$  in the pressure both for systems in the atomic and molecular phases, well within the statistical errors of our CEIMC averages. In principle, the optimal values of the variational parameters could also depend on the specific twist angle. We have checked that this dependence is also within our accuracy; we use a single twist angle in the optimization procedure.

In figure 4 we report the variance per electron, averaged over nuclear sampling, along the T=600K isotherm across the LLPT for systems of  $N_p = 54$  quantum protons. We see that the variance is approximately constant in the two phases, being smaller in the monoatomic-metallic than in the molecular-insulating phase: our trial wave function is slightly more accurate for the atomic liquid. At the transition the variance jumps; this signals the transition. The quality of our present trial wave function can be appreciated by comparing the variance of the present calculation with those in previous CEIMC studies [5, 9]. In ref. [5] we reported

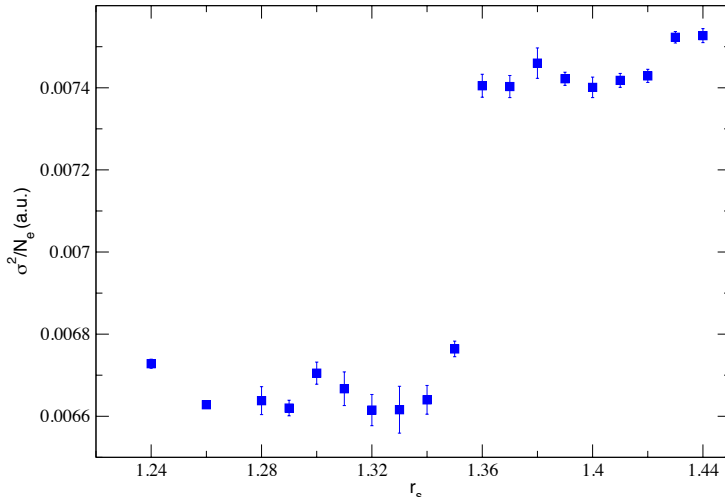


FIG. 4. (color online) Average electronic variance per electron along the  $T=600\text{K}$  isotherm for quantum hydrogen,  $N_p = 54$ . A clear jump is observed at the transition which in this case occur between  $r_s = 1.35$  and  $r_s = 1.36$ .

variances of  $\sim 0.09a.u.$  for monoatomic BCC hydrogen at  $r_s = 1.4$ , while in ref. [9] we reported VMC variances of  $\sim 0.014a.u.$  and  $\sim 0.011a.u.$  for molecular and monoatomic liquid hydrogen at  $T = 600\text{K}$ , respectively. The present improvement is due to algorithmic improvements of our code with the inclusion of the PW solver for the Kohn-Sham orbitals and their representation over a b-spline basis performed by the einspline library [10].

### Nuclear sampling

Improving the variance of the trial wave function is particularly important in CEIMC since smaller variance means more accurate electronic energies and also a smaller noise level resulting in a smaller rejection rate [2], therefore, a larger efficiency of the sampling. Nuclear sampling in this paper is performed by a two level Metropolis scheme [2]. Nuclear forces from DFT are used in a Smart Monte Carlo step [11] at the first level of the sampling, and differences in the energy between QMC and DFT are used to finally accept or reject the new configuration. This scheme allows one to increase the system size while maintaining a reasonable acceptance rate for global nuclear moves. The computational cost of the method still scales as  $N_e^3$ : the cost of computing the Slater determinants during the QMC run. Using DFT forces for prerejection requires one to solve the electronic problem at the DFT level for both the actual and the proposed nuclear configuration. In case of a rejection this is a waste of time with respect to the use of an effective classical nuclear force field but we found this procedure more flexible. In any case the computational load of the DFT part is less than  $\sim 10\%$  of the total computational time. In case of quantum nuclei represented by imaginary time Path Integrals, the sampling is still performed in two steps using the nuclear forces from DFT in the first step, but applied in the space of normal modes of the kinetic action [12, 13]. Working in the normal mode space allows one to select independently the amplitudes of the MC steps for the sampling of path's internal degrees of freedom and the sampling of path's centroid for improved efficiency.

### Reptation Quantum Monte Carlo corrections

Despite the excellent quality of the trial function, VMC introduces a bias on the energy and the pressure, hence on the location of the transition line, since the accuracy of the trial wave function is not the same for

TABLE I. Numerical values of the fitting parameters in eqs. (2) and (3) for two fixed nuclear configurations, one representative of the atomic fluid ( $r_s = 1.34$ ) the other of the molecular fluid ( $r_s = 1.44$ ).

$r_s$	$\alpha_e$	$\gamma_e$	$a_e$	$\alpha_p$	$\gamma_p$	$a_p$
1.34	0.00078(2)	3.7(3)	0.0059(3)	0.0089(4)	1.8(1)	0.48(2)
1.44	0.00108(5)	3.4(3)	0.0027(1)	0.0197(3)	1.7(1)	0.58(1)

both phases. Improved accuracy can be obtained by using a Projection QMC method. Within the fixed-node approximation, the energy is variational but it only depends on the location of the nodal surfaces of the trial wave function or phases for complex trial functions. In CEIMC, the projection method of choice is Reptation Quantum Monte Carlo (RQMC) since it is better adapted to the reweighing procedure embedded in CEIMC [2]. However using RQMC energies in sampling the nuclear configuration space is much more demanding in terms of computational resources. It is much more efficient to generate nuclear trajectories using VMC energies and to estimate the VMC bias on selected, statistically independent, configurations.

RQMC results at fixed nuclear configurations are affected by finite electronic time step  $\tau_e$  and the finite projection time  $\beta_e$  biases. In order to apply RQMC corrections to CEIMC results obtained at the VMC level, we need to establish how to extrapolate RQMC raw data to the zero time step limit  $\tau_e \rightarrow 0$  and to the infinite projection time limit  $\beta_e \rightarrow \infty$ . To this aim we have investigated two configurations, one typical of the atomic liquid ( $r_s = 1.34, T = 1200\text{K}$ ) and the other typical of the molecular liquid ( $r_s = 1.44, T = 1200\text{K}$ ). We performed calculations for several values of the projection time  $\beta_e \in [0, 3]H^{-1}$  and several values of the time step in the range  $\tau_e \in [0.005, 0.015]H^{-1}$ . Our data at given  $\beta_e$  are compatible with a linear dependence of the total energy and of the potential energy with  $\tau_e$ . At fixed  $\tau_e$ , while the total energy per atom  $e$  is monotonously decreasing with  $\beta_e$ , the potential energy per atom  $e_p$  presents a local maximum at short projection time followed by a monotonous decrease with  $\beta_e$ . We globally parametrize our data for total and potential energy as

$$e(\beta_e, \tau_e) = e^\infty(0) + \alpha_e(r_s) e^{-\gamma_e(r_s)\beta_e} + a_e(r_s)\tau_e \quad (2)$$

$$e_p(\beta_e, \tau_e) = e_p^\infty(0) + \alpha_p(r_s) e^{-\gamma_p(r_s)\beta_e} + a_p(r_s)\tau_e. \quad (3)$$

For the potential energy this is a suitable parametrization only at long projection times. The values of the parameters obtained by fitting raw data are reported in table I.

Figure 5 shows for the two configurations, the total and potential energy versus the projection time  $\beta_e$ . The extrapolated value of the pressure is obtained from the extrapolated values of total and potential energy using

$$P^\infty(0) = \frac{2 e^\infty(0) - e_p^\infty(0)}{3v} = \frac{2 e^\infty(0) - e_p^\infty(0)}{4\pi r_s^3} \quad (4)$$

where  $v$  is the volume per particle. For the two configurations considered, the pressure corrections  $\Delta p = p^\infty(0) - p_{vmc}$  are both positive but very small:  $\Delta p(r_s = 1.34) = 1.0(3)\text{GPa}$ ,  $\Delta p(r_s = 1.44) = 1.6(2)\text{GPa}$ .

We use eqs. (2) and (3) to extrapolate our data along all isotherms with the values in table I appropriate to the observed phase. To compute how the thermodynamic properties of the system change as we go from an ensemble of nuclear configurations generated by VMC energies to an ensemble generated by RQMC energies, we use a reweighing technique. The average of a generic observable  $\mathcal{O}(\mathbf{R})$  is

$$\langle \mathcal{O} \rangle_{rqmc} = \frac{\sum_i \mathcal{O}(\mathbf{R}_i) e^{-\beta(E_{rqmc}(\mathbf{R}_i) - E_{vmc}(\mathbf{R}_i))}}{\sum_i e^{-\beta(E_{rqmc}(\mathbf{R}_i) - E_{vmc}(\mathbf{R}_i))}} = \frac{\sum_i \mathcal{O}(\mathbf{R}_i) w_i}{\sum_i w_i} \quad (5)$$

where the sum is over nuclear configurations generated during the CEIMC run with VMC energy. We have used 100 independent nuclear configurations at selected thermodynamic points and for each of them

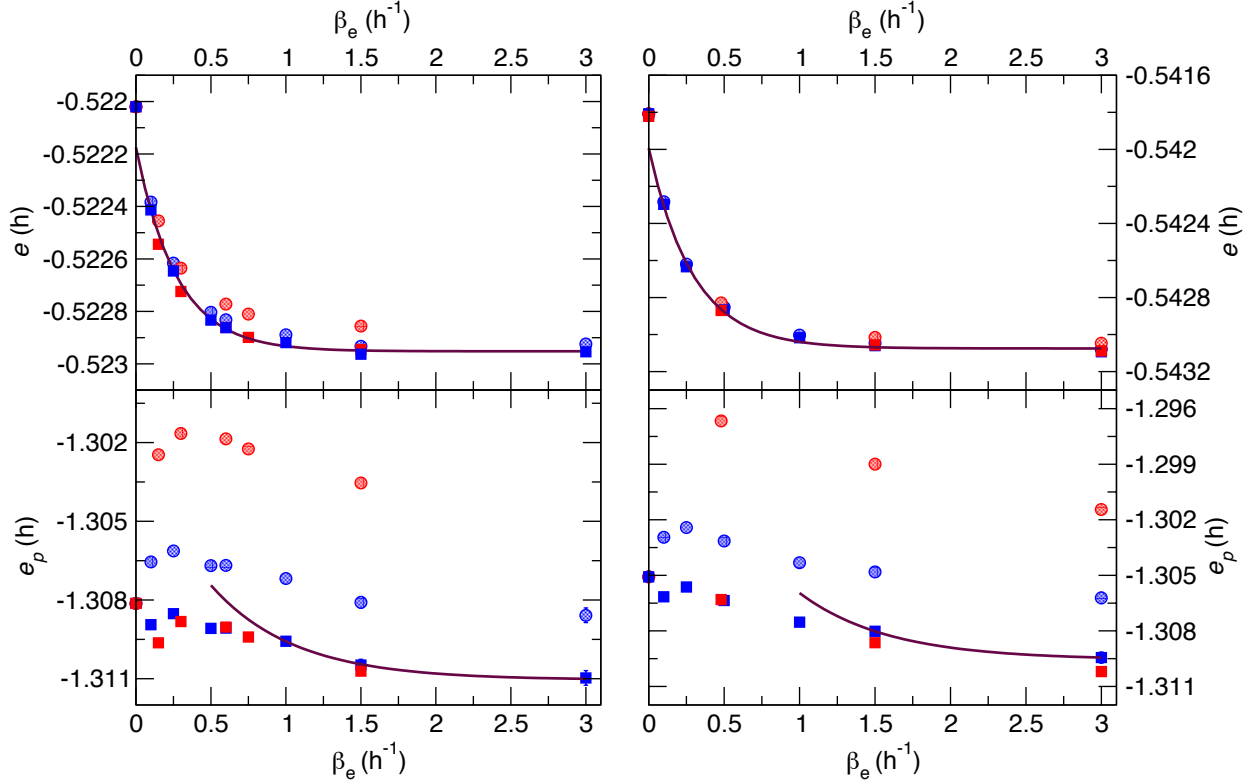


FIG. 5. (color online) Total and potential energy per electron versus RQMC projection time  $\beta_e$  for a liquid atomic nuclear configuration ( $r_s = 1.34$ , left panels) and a liquid molecular nuclear configuration ( $r_s = 1.44$  right panels). The upper panels report the total energy while the lower panels display the potential energy. In each panel blue circles are results obtained with  $\tau_e = 0.005 h^{-1}$  while red circles are results obtained with  $\tau_e = 0.015 h^{-1}$ . Blue and red squares are the same results corrected for the time step error as discussed in the text. The solid curves show the exponential fits to the time step corrected data. Statistical error bars are smaller than the symbols.

recomputed the electronic properties with RQMC and twist-averaged boundary conditions (TABC). The RQMC calculations are performed at a single value of the electronic project time  $\beta_e$  and for a single electronic time step  $\tau_e$  using the same grid of  $4 \times 4 \times 4$  twist angles. Average values are then extrapolated to  $\tau_e \rightarrow 0$  and  $\beta_e \rightarrow \infty$  with the procedure described above. Note that a constant (over configurations) shift of the energy, as the one provided by extrapolation, does not affect the reweighing procedure. In order to establish the significance of the re-weighted results we monitored the statistical efficiency of the weights:

$$N_{eff} = \frac{\sum_i w_i^2}{\sum_i w_i}. \quad (6)$$

This was always found to be at least 75 for 100 configurations indicating that the VMC energies are close enough to the RQMC energies to allow an accurate estimation of the VMC bias. In table II we report results for two densities along the  $T = 1200K$  and  $T = 900K$  isotherms for classical nuclei. At each temperature, the system at the lower density is in the molecular state while the system at the higher density is in the atomic state.

In order to check the sensitivity of our trial wave function to the type of DFT orbitals employed (see below for a more extensive discussion), for the same set of configurations at  $T=900K$ , we repeated the electronic calculation with HSE orbitals. We did not repeat a full RQMC study for several time step and projection time values, but we limit to run RQMC with a single value of  $\tau_e = 0.005$  and  $\beta_e = 0.25$  and use the same

TABLE II. RQMC corrected properties. Energies are in H/atom and pressures are in GPa.

DFT	T(K)	$r_s$	$e^{vmc}$	$e^{rqmc}$	$e^\infty(0)$	$e_p^{vmc}$	$e_p^{rqmc}$	$e_p^\infty(0)$	$P^{vmc}$	$P^\infty(0)$	$P_{sc}^\infty(0)$
PBE	1200	1.34	-0.51592(5)	-0.51670(5)	-0.51679(5)	-1.3083(5)	-1.3042(5)	-1.3120(5)	269(1)	270.9(5)	277(2)
PBE	1200	1.44	-0.53681(6)	-0.53794(5)	-0.53798(5)	-1.3045(5)	-1.2982(5)	-1.3085(5)	180.8(3)	182.3(4)	186(1)
PBE	900	1.32	-0.51435(4)	-0.51483(5)	-0.51515(5)	-1.3211(4)	-1.3207(5)	-1.3252(5)	297.5(4)	300.2(5)	306(1)
PBE	900	1.36	-0.52486(7)	-0.52548(5)	-0.52526(5)	-1.3314(5)	-1.3309(5)	-1.3367(5)	262.2(6)	266.4(6)	271(1)
HSE	900	1.32	-0.51427(5)	-0.51478(5)	-0.51510(5)	-1.3182(4)	-1.3190(5)	-1.3235(5)	294.9(4)	298.5(6)	304(1)
HSE	900	1.36	-0.52396(5)	-0.52507(5)	-0.52552(5)	-1.3231(5)	-1.3260(5)	-1.3349(5)	256.9(5)	264.2(6)	270(1)

extrapolation relations employed in the case of PBE orbitals. However, we re-optimized the variational parameters of the trial function when changing orbitals.

In all cases, RQMC corrections on the total and potential energies are at the level of a few mH/atom. The corrected pressure is found always to be higher than the VMC pressure by roughly half of the finite size correction (see below): the RQMC correction changes the pressures by at most 4 GPa; less than 2% of the absolute value. Comparing results for PBE and HSE orbitals we note that at the VMC level, HSE total and potentials energies are slightly higher than the corresponding PBE values. At the RQMC level after the extrapolations, this difference is recovered for the total energy but not quite for the potential energy, and this results in small differences in the total pressure, of the order of 2 GPa. The recovery on the total energy demonstrates again the accuracy and flexibility of our trial wave function. The residual effect on the potential energy and pressure might come from the extrapolation procedure which might be slightly less accurate for the potential energy than for the total energy, in particular since the RQMC runs have only been performed for a short projection time. Since the effect is small we did not performed a complete RQMC study with HSE orbitals.

In the last column of table II we report the final estimate of the pressure after both RQMC and size corrections (SC) have been added. Those corrections are both positive and globally increase VMC data by roughly 7-8 GPa in the atomic phase and 4-7 GPa in the molecular phase.

### Orbital bias

In this section we consider another kind of bias which could affect our results: the orbital bias. Indeed in our present protocol the orbitals are obtained from the DFT solver and not re-optimized in presence of the Jastrow and the backflow terms, although the latter contribution effectively changes the orbitals. Therefore it is legitimate to ask how much the results depend on the specific form of the DFT orbitals adopted. In the past we have already found that in a perfect hydrogen crystal (Pbcn structure at 300GPa) the orbital bias is negligible [6]. Here we reconsider the question by computing the electronic properties of two fixed nuclear configurations, one molecular liquid ( $r_s = 1.49, T = 1200\text{K}$ ) and the other atomic liquid ( $r_s = 1.34, T = 1200\text{K}$ ) with the following type of orbitals: LDA, GGA-PBE, BLYP, vdW-DF and vdW-DF2. These are some of the X-C approximations in DFT recently benchmarked against QMC results [14]. We only use VMC calculations since we have seen above and in ref. [6] that convergence with electronic projection time for different orbitals is very similar: the RQMC results mimic the VMC ones. In figure 6, for both nuclear configurations, we report total energy and variance for the various orbital types. For all types of orbitals we report values obtained with only the analytical part of the Jastrow and the backflow. In addition for PBE, LDA and vdW-DF2, we report results for the full trial function with the optimized correlation and backflow. As discussed above we see that optimizing the trial function decreases the energy by roughly 1mH/atom and the variance by 40% at both densities. Comparing the cases with the analytic wave function, we observe that for both configurations the trial function with PBE orbitals provides the lowest energy and variance, but the differences with LDA, BLYP and vdW-DF are quite limited (within 0.2mH/atom for the energy and 1mH<sup>2</sup>/atom for the variance). However vdW-DF2 orbitals provide markedly higher energies (by

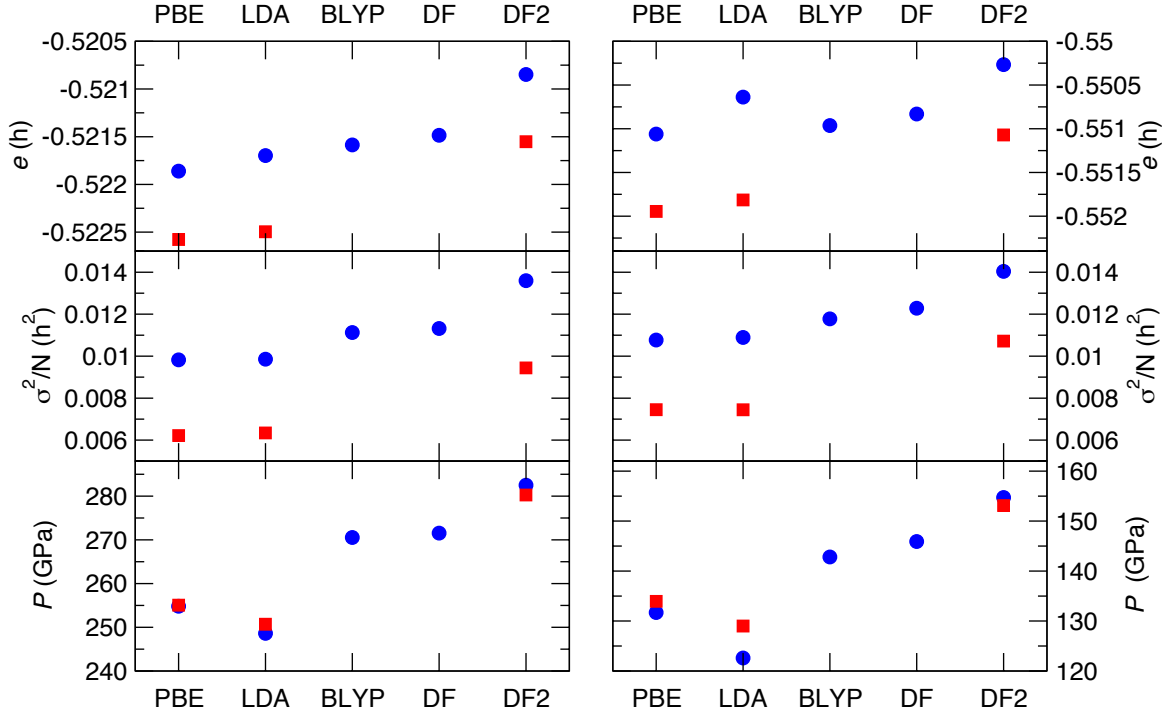


FIG. 6. (color online) Single nuclear configuration energy (upper panels), variance (middle panels) and pressure (lower panels) from various kind of orbitals as indicated on the abscissa. The left panels refers to a typical atomic configuration ( $r_s = 1.34$ ) while the right panels correspond to a typical molecular configuration ( $r_s = 1.49$ ). For PBE, LDA and vdW-DF2 we show both the SJ results with the analytical form of the trial function (blue circles) and the results when the correlation and backflow terms are optimized (red squares), while for BLYP and vdW-DF only results for the analytical form are reported (blue circles). Statistical error bars are smaller than the symbols.

roughly 1mH/atom) and larger variances. We see that this difference is not reduced if the wave functions is optimized. We conclude that our results are largely independent of the orbitals with the noticeable exception of vdW-DF2 orbitals. However, the PBE orbitals provide the best type of orbitals for the conditions of the LLPT. The dependence of the pressure on the orbitals is illustrated in the lower panels of the figure. The orbitals influence the pressure more significantly with the LDA form providing the lowest pressure,  $\sim 5$ GPa lower, while the vdW-DF2 gives the highest pressure,  $\sim 25 - 30$  GPa higher than our best estimate of the pressure provided by the PBE orbitals with fully optimized wave functions.

To better establish how much different type of orbitals will bias our final estimate of the LLPT transition we have performed full CEIMC calculations with vdW-DF2 orbitals at various densities along the  $T=1200$ K isotherm. In figure 7 we compare the EOS along the  $T=1200$ K isotherm and across the LLPT from trial functions with vdW-DF2 orbitals and with PBE orbitals. We see that the transition occurs at the same densities but the pressure from vdW-DF2 orbitals is larger than the pressure from PBE by roughly 25GPa. Recall that within DFT theory these approximations provide a pressure shift for the transition of roughly 200 GPa, almost an order of magnitude larger than the sensitivity of pressure within QMC.

### Convergence with the number of twists

Our simulations have been performed using a  $4 \times 4 \times 4$  grid of twists irrespectively of the size of the systems considered. For systems of the smallest size (54 protons) we have checked that this choice provides total

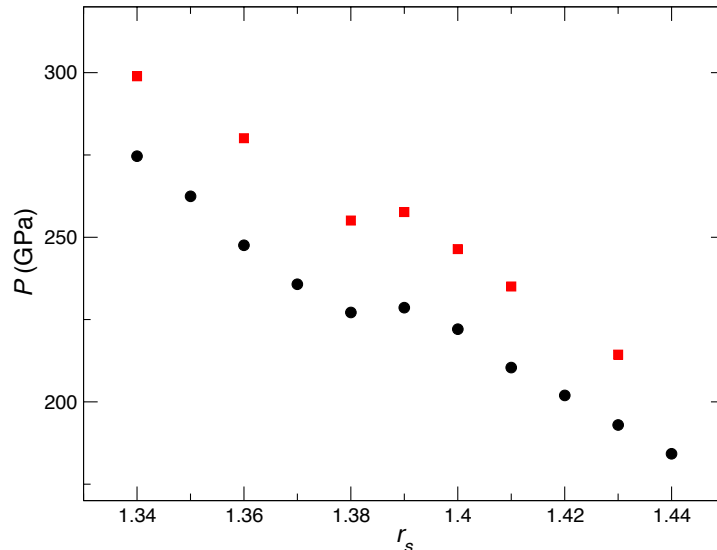


FIG. 7. (color online) EOS from VdW-DF2 (red squares) and PBE (black circles) based, fully optimized, trial wavefunction. Statistical error bars are smaller than the symbols.

electronic energies which differs by less than 0.025 mH/atom from the fully converged value (extrapolated). For the pressure, the deviation from the extrapolated value was smaller than 0.1 GPa.

### Convergence of the nuclear path integral

Another possible bias in our calculation is related to the use of a finite number of time slices  $P$  in representing the quantum nuclei by imaginary time path integrals. We need to study the dependence of the results on the nuclear time step  $\tau_p = \beta/P$  since increasing the number of time slices requires more computer resources. As explained in ref [2], in order to reduce the number of proton slices we introduce a pairwise effective classical potential for which we can compute the pair action [1] and treat the difference between the electronic energy and the effective potential energy with the “primitive approximation”. For reasonable effective potentials, obtained for instance from the proton-proton  $g(r)$  by the Boltzmann Inversion procedure [19], this method requires a proton time step of  $\tau_p \leq 66H^{-1}$  which allows us to use  $P = 4$  at  $T=1200\text{K}$ , and  $P = 8$  at  $T=600\text{K}$ , despite that along a single isotherm the system undergoes a dissociation transition. In order to check that those values are indeed sufficient for accurate predictions we have repeated the calculations along the  $T=600\text{K}$  isotherm using 4, 8 and 16 slices. The results are shown in fig. 8. We clearly see that the systems with  $P = 4$  presents a transition pressure significantly higher than in the cases of  $P = 8$  and  $P = 16$ . Those are found to be in agreement with each other, indicating that 8 time slices is enough at  $T=600\text{K}$  within the present statistical error.

### Size effects

As mentioned in the main text, we employ twist-averaged boundary conditions (TABC) during the nuclear sampling. This removes the largest size effects in fermionic quantum Monte Carlo [15]. To illustrate how large the effect of TABC on the nuclear sampling is, we compare in figure 9 the proton-proton  $g_{pp}(r)$  for the same system of 54 protons at  $r_s = 1.44$  and  $T=600\text{K}$  for a sampling using electronic energy at the  $\Gamma$  point only and a sampling using a  $4 \times 4 \times 4$  grid of twist angles. The observed liquid structure is markedly different

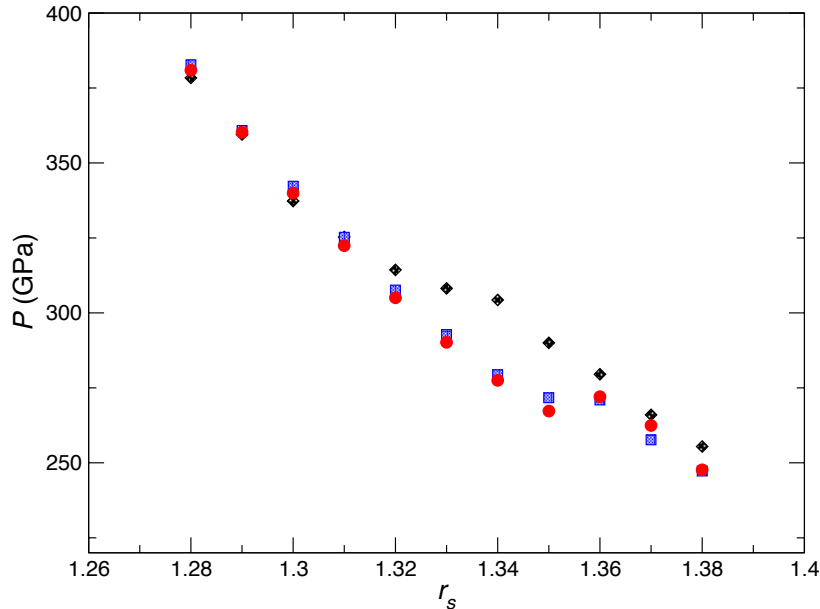


FIG. 8. (color online) EOS along the  $T=600\text{K}$  isotherm and across the LLPT for quantum protons with  $P = 4$  (black diamonds),  $P = 8$  (red circles) and  $P = 16$  (blue squares). Statistical error bars are smaller than the symbols.

with a much reduced molecular peak when using  $\Gamma$  point energies. The nuclear system is frustrated by the imposed insulating character of the electronic liquid (a 54 electrons system corresponds to a closed shell in the reciprocal space in 3D) and not able to form proper molecules. On the other hand the use of TABC energies removes such constraint and drives the system toward its equilibrium state. Note how similar the observed  $g_{pp}(r)$  with  $\Gamma$  point energies is to the one reported in ref [17] (see figure 3 of the Supplemental Material). As concerns thermodynamic properties, the average internal energy is lower by 15mH/atom when using electrons at the  $\Gamma$  point, a usual results for closed shell systems [15]. The change in pressure between the two systems is also dramatic: the system with  $\Gamma$  point electrons has a pressure of  $P = 116.7(1)$  GPa while the system with TABC electrons has a pressure of  $P = 177.3(1)$  GPa, a pressure jump larger than the one observed in ref. [16] when going from systems of 64 to 256 protons with  $\Gamma$  point electrons. This analysis suggests that the differences between the results of that investigation and our present results might be mainly related to the different treatment of size effects during the sampling of the nuclear configuration space.

Residual size corrections to our predictions for the internal energy and pressure are computed following ref [18] and added to the raw data (see numerical tables in the last section of this Supporting Information).

To check that size effects are not a major issue in our study we have simulated larger systems of  $N_p = N_e = 128$  at four densities and  $T=1200\text{K}$ . In figure 10 we compare the proton-proton  $g(r)$  for the two system sizes at the four densities. The agreement at the highest ( $r_s = 1.34$ ) and the lowest ( $r_s = 1.44$ ) densities is remarkable, showing that the local structure of the liquid far from the transition point is captured already with  $N_p = 54$  protons. Closer to the transition, occurring here between  $r_s = 1.38$  and  $r_s = 1.39$ , the agreement is less good; the larger system appears to exhibit a sharper transition. Indeed we observe that at  $r_s = 1.37$  the smaller system still presents some molecular character not seen in the larger system. On the other side of the transition, at  $r_s = 1.40$ , the molecular character is more pronounced in the larger system. However the effect is quite small and could also be related to the finite sampling since fluctuations are larger near phase boundaries, in particular for the smaller system, and properties converge much slower than away from the transition.

Finally we want to discuss finite size effects on the conductivity and  $\Gamma_\rho$ , the integral of the off-diagonal

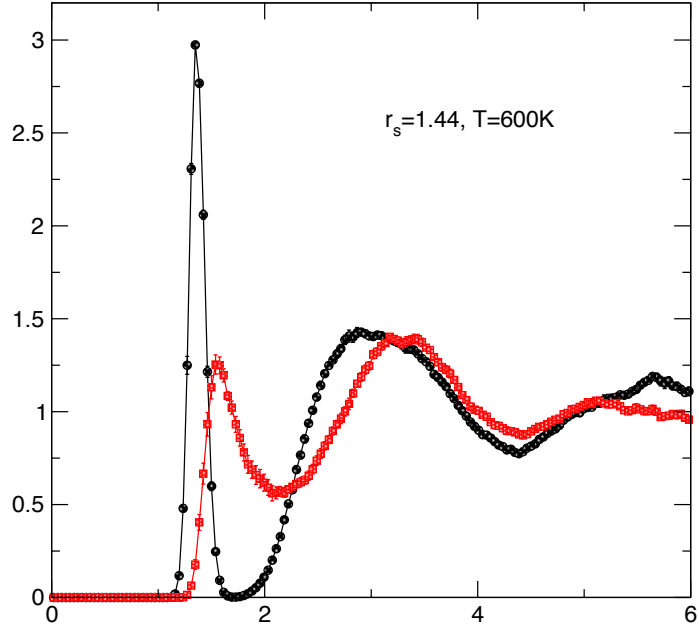


FIG. 9. (color online) Proton-proton  $g(r)$  at  $r_s = 1.44$ ,  $T=600\text{K}$  and  $N_p = 54$  classical protons. Comparison between CEIMC sampling with TABC electronic energy (black circles) and CEIMC sampling with  $\Gamma$  point electronic energy only (red squares).

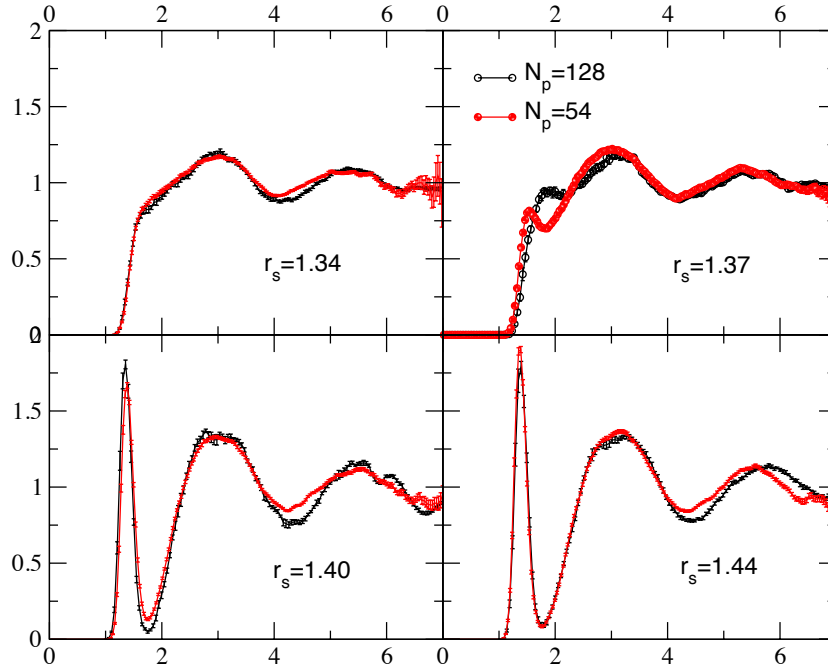


FIG. 10. (color online)  $T=1200\text{K}$  with classical protons. Comparison between  $g_{pp}(r)$  for  $N_p = 54$  (red filled circles) and  $N_p = 128$  (black open circles) at various densities around the transition.

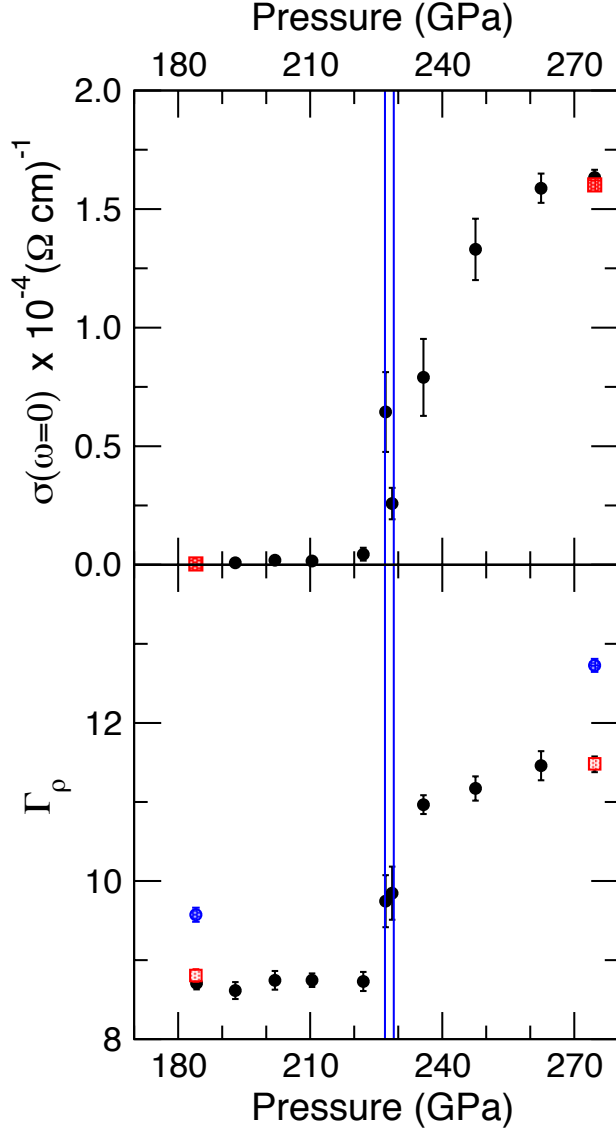


FIG. 11. (color online)  $T=1200\text{K}$  classical protons. DC conductivity (upper panel) and electron localization parameter  $\Gamma_\rho$  (lower panel) versus pressure. Blue vertical lines indicates the transition as detected by the jump in specific volume. Optical calculations are performed with PBE orbitals. Data for  $N_p = 54$  (black circles) and  $N_p = 128$  (blues circles and red squares) are compared. The difference between blue circles and red squares is only in the upper integration limit.

single-electron density matrix. In figure 11 we compare results for systems of 54 and 128 protons for the DC conductivity (upper panel) and for  $\Gamma_\rho$  (lower panel). Differences in the conductivity are negligible (here we use the PBE approximation in the optical calculation) while are more evident on  $\Gamma_\rho$ . However the deviations on  $\Gamma_\rho$  arise from the different upper limit of the integral for the systems with different sizes rather than from a difference in the integrand function. Limiting the two integrals at the same upper cutoff radius we observe a perfect agreement (see red squares in panel b) between the two investigated system sizes, which shows that residual size effects after TABC are negligibly small.

### Numerical data

In this last section we report CEIMC data for internal energy and pressure relative to the experiments performed along the five isotherms for both systems with quantum and classical protons. Raw and size-corrected data are reported except at  $T=3000\text{K}$ .

TABLE III. CEIMC-VMC estimates of the internal energy and pressures, at  $T = 3000\text{K}$ . Only classical protons have been considered at this temperature.

$r_s$	$\rho(\text{gcm}^{-3})$	$e(\text{h/at})$	P(GPa)
1.44	0.902885	-0.51920(6)	174(2)
1.52	0.767696	-0.5285(1)	117.2(3)
1.55	0.723977	-0.5317(2)	102.8(5)
1.58	0.683516	-0.5349(2)	91.0(5)
1.59	0.6707	-0.5366(3)	88.8(7)
1.60	0.658203	-0.5383(3)	87.8(8)
1.61	0.646014	-0.5387(3)	83.3(7)
1.62	0.634125	-0.5405(4)	84.4(8)
1.63	0.622525	-0.5417(3)	79.8(6)
1.64	0.611207	-0.5430(3)	77.3(6)
1.65	0.600161	-0.5439(2)	74.8(3)
1.66	0.58938	-0.5451(1)	72.1(2)
1.70	0.548748	-0.5483(1)	62.3(2)

TABLE IV. CEIMC-VMC estimates of the internal energy and pressures, at  $T = 1500\text{K}$ . Both classical and quantum protons have been considered at this temperature.

$r_s$	$\rho(\text{gcm}^{-3})$	$e_{cl}(\text{h/at})$	$P_{cl}(\text{GPa})$	$e_{cl}^{sc}(\text{h/at})$	$P_{cl}^{sc}(\text{GPa})$	$e_q(\text{h/at})$	$P_q(\text{GPa})$	$e_q^{sc}(\text{h/at})$	$P_q^{sc}(\text{GPa})$
1.39	1.00387	-0.5230(1)	210.2(5)	-0.5181(1)	214.4(5)	—	—	—	—
1.40	0.982507	-0.5245(1)	198.7(5)	-0.5196(1)	203.0(5)	-0.5224(2)	200.7(6)	-0.5175(2)	205.0(6)
1.41	0.961751	-0.5268(4)	192.8(3)	-0.5219(4)	197.1(3)	-0.5236(3)	191(1)	-0.5187(3)	195(1)
1.42	0.941575	-0.5287(2)	185(1)	-0.5243(2)	189(1)	-0.5251(2)	181(1)	-0.5203(2)	185(1)
1.43	0.921959	-0.5323(2)	188(1)	-0.5278(2)	191.8(9)	-0.5266(6)	173(1)	-0.5217(6)	178(1)
1.44	0.902885	-0.5338(1)	180(1)	-0.5293(1)	183(1)	-0.5287(2)	164(1)	-0.5238(2)	168(1)
1.45	0.884333	-0.53600(9)	173.3(3)	-0.5314(1)	176.9(4)	-0.5306(2)	163(1)	-0.5257(2)	168(1)
1.46	0.866286	—	—	—	—	-0.5350(2)	165.1(8)	-0.5305(2)	168.8(8)
1.47	0.848727	—	—	—	—	-0.5353(3)	159.1(7)	-0.5307(3)	162.7(7)

TABLE V. CEIMC-VMC estimates of the internal energy and pressures, at  $T = 1200\text{K}$ . Both classical and quantum protons have been considered at this temperature.

$r_s$	$\rho(\text{gcm}^{-3})$	$e_{cl}(\text{h/at})$	$P_{cl}(\text{GPa})$	$e_{cl}^{sc}(\text{h/at})$	$P_{cl}^{sc}(\text{GPa})$	$e_q(\text{h/at})$	$P_q(\text{GPa})$	$e_q^{sc}(\text{h/at})$	$P_q^{sc}(\text{GPa})$
1.34	1.12048	-0.51592(7)	269(1)	-0.51065(7)	275(1)	-0.5130(1)	273.7(4)	-0.5077(1)	278.9(4)
1.35	1.09577	-0.51813(8)	257.7(6)	-0.51313(8)	262.4(6)	-0.5143(1)	261.0(6)	-0.5093(1)	265.7(6)
1.36	1.07177	-0.5198(1)	243.1(5)	-0.5148(1)	247.6(5)	-0.5162(1)	250.1(6)	-0.5112(1)	254.5(6)
1.37	1.04848	-0.5220(1)	232.5(7)	-0.5171(1)	236.9(7)	-0.5189(1)	234.9(6)	-0.5140(1)	239.3(6)
1.38	1.02585	-0.5256(2)	234.1(2)	-0.5208(2)	238.2(2)	-0.5203(1)	224.2(5)	-0.5155(1)	228.3(5)
1.39	1.00387	-0.5270(2)	224(1)	-0.5224(2)	227(1)	-0.5224(1)	211.9(6)	-0.5178(1)	215.7(6)
1.40	0.982507	-0.5301(1)	218.5(4)	-0.5257(1)	222.1(4)	-0.5239(1)	202.7(7)	-0.5195(1)	206.3(7)
1.41	0.961751	-0.53175(9)	206.9(4)	-0.5273(1)	210.4(4)	-0.5258(1)	194.9(7)	-0.5214(1)	198.4(7)
1.42	0.941575	-0.53353(6)	198.5(3)	-0.52913(6)	202.0(3)	-0.5290(1)	199.8(5)	-0.5248(1)	203.4(5)
1.43	0.921959	-0.5354(1)	189.5(4)	-0.5310(1)	193.0(4)	-0.5314(1)	192.6(6)	-0.5266(1)	196.1(6)
1.44	0.902885	-0.53684(8)	180.8(3)	-0.53243(8)	184.2(3)	-0.5326(1)	185.3(5)	-0.5282(1)	188.8(5)

TABLE VI. CEIMC-VMC estimates of the internal energy and pressures, at  $T = 900\text{K}$ . Both classical and quantum protons have been considered at this temperature.

$r_s$	$\rho(\text{gcm}^{-3})$	$e_{cl}(\text{h/at})$	$P_{cl}(\text{GPa})$	$e_{cl}^{sc}(\text{h/at})$	$P_{cl}^{sc}(\text{GPa})$	$e_q(\text{h/at})$	$P_q(\text{GPa})$	$e_q^{sc}(\text{h/at})$	$P_q^{sc}(\text{GPa})$
1.30	1.22712	-0.50989(3)	332.2(5)	-0.50445(3)	337.7(5)	—	—	—	—
1.32	1.17219	-0.51435(4)	297.5(4)	-0.50892(4)	303.0(4)	—	—	—	—
1.33	1.14595	-0.5167(1)	284(1)	-0.5114(1)	290(1)	—	—	—	—
1.34	1.12048	-0.5190(1)	272.3(7)	-0.5137(1)	277.6(7)	—	—	—	—
1.35	1.09577	-0.5210(1)	257(1)	-0.5157(1)	263(1)	—	—	—	—
1.36	1.07177	-0.52486(7)	262.2(6)	-0.51989(7)	266.7(6)	-0.5192(2)	242.0(8)	-0.5137(2)	247.5(8)
1.37	1.04848	-0.52662(7)	246.6(5)	-0.52167(7)	251.2(5)	—	—	—	—
1.38	1.02585	—	—	—	—	-0.5231(1)	220.9(3)	-0.5176(1)	226.4(3)
1.39	1.00387	-0.53098(6)	227.6(3)	-0.52604(6)	232.2(3)	-0.5248(3)	213(1)	-0.5193(3)	218(1)
1.40	0.982507	—	—	—	—	-0.5272(2)	203(1)	-0.5218(2)	208(1)
1.41	0.961751	—	—	—	—	-0.5297(2)	208.2(8)	-0.5247(2)	212.8(2)
1.42	0.941575	—	—	—	—	-0.5313(1)	199.5(8)	-0.5263(1)	204.1(8)
1.43	0.921959	—	—	—	—	-0.5325(1)	189.3(8)	-0.5276(1)	193.9(8)
1.45	0.884333	—	—	—	—	-0.5351(1)	173.3(4)	-0.5302(1)	177.9(4)

- 
- [1] Ceperley D. M., Path integrals in the theory of condensed helium. *Rev. Mod. Phys.* **67**, 279-356 (1995).  
[2] Pierleoni C. and Ceperley D. M., The Coupled Electron-Ion Monte Carlo Method, *Lecture Notes in Physics* **703**, 641-683 (2006).  
[3] Tubman N. M., Liberatore E., Pierleoni C., Holzmann M., and Ceperley D. M., Molecular-Atomic Transition along the Deuterium Hugoniot Curve with Coupled Electron Ion Monte Carlo Simulations, *Phys. Rev. Letts.* **115**, 045301 (2015).  
[4] Holzmann, M., Ceperley D. M., Pierleoni C., and Esler K., Backflow Correlations for the Electron Gas and Metallic Hydrogen, *Phys. Rev. E* **68**, 046707 (2003).  
[5] Pierleoni C., Delaney K. T., Morales M. A., Ceperley D. M., and Holzmann M., Trial wave functions for High Pressure Metallic Hydrogen, *Comp. Phys. Comm.* **179**, 89-97 (2008).  
[6] Morales M. A., Clay R., Pierleoni C., and Ceperley D. M., First Principles Methods: A perspective from Quantum Monte Carlo. *Entropy* **16**, 287-321 (2014).

TABLE VII. CEIMC-VMC estimates of the internal energy and pressures, at  $T = 600\text{K}$ . Both classical and quantum protons have been considered at this temperature.

$r_s$	$\rho(\text{g cm}^{-3})$	$e_{cl}(\text{h/at})$	$P_{cl}(\text{GPa})$	$e_{cl}^{sc}(\text{h/at})$	$P_{cl}^{sc}(\text{GPa})$	$e_q(\text{h/at})$	$P_q(\text{GPa})$	$e_q^{sc}(\text{h/at})$	$P_q^{sc}(\text{GPa})$
1.24	1.41402	-0.49644(4)	460(1)	-0.49089(4)	466(1)	-0.4916(1)	472.0(7)	-0.4860(1)	478.1(7)
1.26	1.34774	-0.50221(6)	411.1(7)	-0.49666(6)	417.3(7)	-0.4976(1)	419.9(5)	-0.4920(1)	426.0(5)
1.27	1.31616	-0.50448(4)	388.0(7)	-0.49894(4)	394.1(7)	—	—	—	—
1.28	1.28555	-0.50738(4)	368.5(4)	-0.50183(4)	374.6(4)	-0.5021(1)	375.5(6)	-0.4965(1)	381.6(6)
1.29	1.25589	-0.50993(8)	349.8(8)	-0.50443(8)	355.7(8)	-0.50481(7)	354.8(5)	-0.49931(8)	360.7(5)
1.30	1.22713	-0.51218(5)	328.7(4)	-0.50649(5)	335.0(4)	-0.5078(3)	334.8(7)	-0.5021(3)	341.1(7)
1.31	1.19924	-0.51612(7)	331(1)	-0.51072(7)	337(1)	-0.5124(2)	317.1(8)	-0.5042(2)	323.0(8)
1.32	1.17219	-0.51886(5)	319.5(6)	-0.51346(5)	325.4(6)	-0.5111(2)	300.2(4)	-0.5070(2)	306.1(4)
1.33	1.14595	-0.52142(7)	303.8(9)	-0.51602(7)	309.7(9)	-0.5140(2)	285.9(7)	-0.5086(2)	291.8(7)
1.34	1.12048	-0.52335(5)	289(1)	-0.51796(5)	294(1)	-0.5160(1)	273.8(4)	-0.5106(1)	279.4(4)
1.35	1.09577	-0.52537(4)	274.5(7)	-0.51997(4)	279.8(7)	-0.5177(2)	261.0(6)	-0.5123(2)	266.3(6)
1.36	1.07177	-0.52768(9)	262.5(5)	-0.52228(9)	267.5(5)	-0.5212(1)	269.3(4)	-0.5164(1)	273.6(4)
1.37	1.04848	-0.52980(4)	249.2(4)	-0.52440(4)	253.9(4)	-0.5232(1)	259.3(3)	-0.5184(1)	263.6(3)
1.38	1.02585	-0.53188(6)	237.7(5)	-0.52712(6)	241.9(6)	-0.5259(1)	244.1(5)	-0.5211(1)	248.4(5)
1.39	1.00387	-0.53385(3)	227.1(4)	-0.52909(3)	231.3(4)	-0.52794(8)	230.0(3)	-0.52318(8)	234.4(3)
1.40	0.98251	-0.53556(2)	216.1(4)	-0.53080(2)	220.3(4)	-0.5295(1)	218.7(6)	-0.5247(1)	223.0(6)
1.41	0.96175	-0.53733(6)	205.4(4)	-0.53257(6)	209.6(4)	-0.5315(1)	208.2(3)	-0.5267(1)	212.5(3)
1.42	0.94157	-0.53906(5)	195.2(3)	-0.53429(5)	199.4(3)	-0.5332(2)	197.8(4)	-0.5284(2)	202.0(4)
1.43	0.92196	-0.54061(5)	185.1(3)	-0.53585(5)	189.4(3)	-0.5355(2)	189.8(4)	-0.5307(2)	194.1(4)
1.44	0.90288	-0.54209(6)	177.3(3)	-0.53733(6)	181.6(3)	-0.5366(1)	182.2(4)	-0.5318(1)	186.5(4)
1.45	0.884333	-0.54386(7)	168.9(2)	-0.53909(6)	173.2(2)	—	—	—	—
1.46	0.866286	-0.54541(5)	161.5(2)	-0.54064(5)	165.8(2)	—	—	—	—
1.47	0.848727	-0.54684(7)	153.6(3)	-0.54207(7)	157.9(3)	—	—	—	—
1.48	0.831639	-0.54834(5)	145.8(2)	-0.54358(5)	150.1(2)	—	—	—	—
1.49	0.815007	-0.54960(5)	137.8(3)	-0.54484(5)	142.1(3)	—	—	—	—
1.50	0.798815	-0.55095(4)	132.5(2)	-0.54619(4)	136.7(2)	—	—	—	—

- [7] Giannozzi P., Baroni S., et al., QUANTUM ESPRESSO: a modular and open-source software project for quantum simulations of materials, *J. Phys. Cond. Mat.* **21**, 395502 (2009).
- [8] Ceperley D. M., Dewing M., and Pierleoni C., The Coupled Electronic-Ionic Monte Carlo Simulation Method, *Lecture Notes in Physics* **605** 473-500 (2002).
- [9] Liberatore E., Morales M.A., D.M. Ceperley, and Pierleoni C., Free energy methods in coupled electron ion Monte Carlo, *Mol. Phys.* **109**, 3029 (2011).
- [10] Esler K. P., <http://einspline.sourceforge.net>.
- [11] Allen M.P and Tildesley D., Computer Simulation of Liquids, Oxford University Press (1987).
- [12] Cao J and Berne B. J., A Born–Oppenheimer approximation for path integrals with an application to electron solvation in polarizable fluids, *J. Chem. Phys.* **99**, 2902 (1993).
- [13] Tuckermann, M.E., Statistical Mechanics: Theory and Molecular Simulation; Oxford University Press: Oxford, UK (2010).
- [14] Clay R.C. III, Mcminis J., McMahon J.M., Pierleoni C., Ceperley D.M., and Morales M.A., Benchmarking exchange-correlation functionals for hydrogen at high pressures using quantum Monte Carlo, *Phys. Rev. B* **89**, 184106 (2014).
- [15] Lin C., Zong F.-H. and Ceperley D. M., Twist-averaged boundary conditions in continuum Quantum Monte Carlo algorithms, *Phys. Rev. E* **64**, 016702 (2001).
- [16] Mazzola G, Yunoki S., and Sorella S, Unexpectedly high pressure for molecular dissociation in liquid hydrogen by electronic simulation, *Nature Comm.* **5**, 3487 (2014).

- [17] Mazzola G and Sorella S., Distinct Metallization and Atomization Transitions in Dense Liquid Hydrogen, *Phys. Rev. Letts.* **114** 105701 (2015).
- [18] Holzmann M., Clay R.C. III, Morales M.A., Tubman N.M., Ceperley D.M., and Pierleoni C., Theory of Finite Size Effects for Electronic Quantum Monte Carlo Calculations of Liquids and Solids, <http://arxiv.org/abs/1603.03957> (2016).
- [19] Müller-Plathe F., Coarse-Graining in Polymer Simulation: From the Atomistic to the Mesoscopic Scale and Back, *Chem. Phys. Chem.* **3**, 754 (2002); Reith D., Pütz M. and Müller-Plathe F., Deriving effective mesoscale potentials from atomistic simulations, *J. Comput. Chem.* **24**, 1624 (2003).